

Melting Coulomb clusters through nonreciprocity-enhanced parametric pumping

Zhicheng Shu,¹ Wei-Chih Li,¹ Wentao Yu,² and Justin C. Burton^{1,*}

¹*Department of Physics, Emory University, Atlanta, GA 30322*

²*Applied Physics and Materials Science, California Institute of Technology, Pasadena, CA 91125*

(Dated: February 19, 2026)

Complex systems out of equilibrium often experience intermittent oscillations between quiescent and highly dynamic states. The type of intermittency depends on how energy is pumped into the system, and how it is dissipated. While intermittency is usually driven by stochastic noise or external forcing, energy can also be sourced from field-mediated interactions between particles, which are often nonreciprocal and effectively violate Newton’s 3rd law. Here we demonstrate how nonreciprocal interactions produce intermittency in clusters of charged micron-sized particles confined in a plasma sheath. Through three-dimensional particle tracking, we observe that vertical oscillations, induced by fluctuations of the plasma environment, can be parametrically coupled to the horizontal modes. Experiments and simulations show that nonreciprocal interactions strongly amplify this parametric coupling, creating a positive feedback loop that drives explosive growth of both the horizontal and vertical modes. This mechanism triggers abrupt melting transitions from an ordered cluster to an ergodic gas-like state, and leads to intermittent switching between states over long time scales. Overall, our work identifies nonreciprocal interactions as a key mechanism through which strongly coupled finite systems transform interaction-mediated activity into dynamical nonequilibrium states.

I. INTRODUCTION

Understanding how systems organize and function far from equilibrium remains one of the central challenges in statistical and soft matter physics. Nonequilibrium systems typically break detailed balance, continuously extract energy from their surroundings, and sustain entropy production [1, 2]. As a result, they can exhibit dynamics and functionalities that are inaccessible in equilibrium. Nonequilibrium systems are ubiquitous in nature, spanning length scales from molecular motors to animal flocks [3–8]. Similar principles are increasingly exploited in the laboratory to design synthetic materials, including colloidal assemblies that self-organize into dynamical structures [9–16] and active materials composed of work-generating units that support self-excited oscillations and locomotion [17–22].

A many-body system of interacting particles can be driven far from equilibrium by making each particle active. Here, “activity” typically means that individual constituents internally consume energy to generate motion [1, 23, 24]. In nature, microswimmers such as *E. coli* convert chemical energy from ATP hydrolysis into self-propulsion [24, 25]. Nonliving particles can acquire autonomous motion when energy is supplied externally through phoretic mechanisms such as light activation [9, 10], chemical reactivity [26, 27], or DC electric fields [11–13]. Collections of such self-propelled units are referred to as active matter, which exhibits emergent behavior arising from their persistent energy consumption at the single-particle level, while the interactions between particles can be pairwise and reciprocal [23].

Even without single-particle activity, interacting particles can exhibit rich collective behavior when the interactions themselves become nonreciprocal, i.e., $\mathbf{F}_{ij} \neq -\mathbf{F}_{ji}$, effectively violating Newton’s 3rd law [28, 29]. Such nonreciprocity naturally arises when forces are mediated through a driven environment. For example, wave-mediated interactions can support emergent collective activity, allowing two or more otherwise passive particles to harness energy from scattered waves and move coherently [30, 31]. This “social activity” depends strongly on the spatial configuration of particles, and will generally involve non-pairwise interactions [32–34]. In fact, many living systems that exhibit flocking, schooling, and other coordinated motion involve both single particle activity and nonreciprocal, field-mediated interactions [23, 35–37].

Significant progress has been made in understanding collective behavior from nonreciprocity in the thermodynamic limit, such as the emergence of spatiotemporal oscillations and dynamical patterns that are inaccessible in equilibrium systems [38–46]. However, much less is known about how nonreciprocity affects the dynamics of finite systems with only a few coupled degrees of freedom where coarse-grained descriptions become insufficient. For such systems, analytical and numerical results have shown that nonreciprocity alone can break detailed balance and induce energy and information flow [29, 47, 48]. However, experimental data remains limited, particularly when steady states do not exist, and dynamics are complex.

In this work, we experimentally demonstrate that nonreciprocal interactions between just two particles can generate unique nonequilibrium states marked by intermittent bursts of activity that drive transitions between quiescent and dynamical phases. Our experiments use a tractable model system: charged microparticles con-

* justin.c.burton@emory.edu

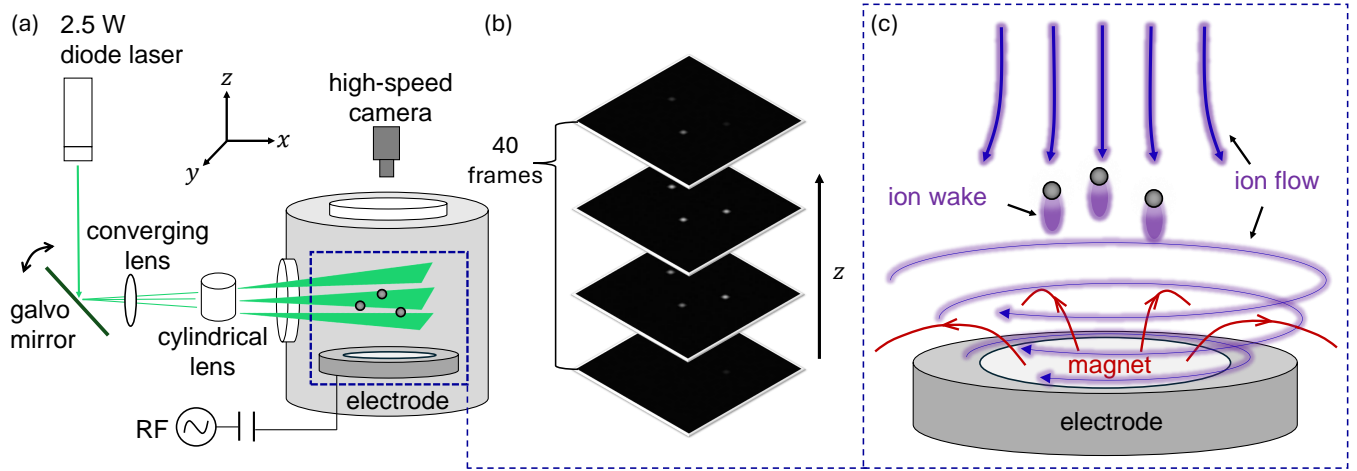


FIG. 1. Sample preparation and imaging of dusty plasma clusters. (a) Schematic of the plasma chamber and the laser tomographic imaging. Micron-sized dust particles are dropped into the argon plasma discharge in the chamber. The high speed camera is synchronized with a scanning laser sheet which illuminates particles at different height. (b) A stack of 40 frames of images are captured within one cycle of laser scan, where particles at different z positions are illuminated in different frames. (c) The charged dust particles are levitated above the electrode and confined within the center of the electrode due to the electric field gradient. The ions stream towards the electrode and form the ion wakes below the particles which make the interactions between particles effectively nonreciprocal. The down-streaming ions also drift in the azimuthal direction due to the magnetic field, which induces the cluster rotation. Note that the ion drift velocity is much smaller than the streaming velocity.

fined in a plasma sheath, commonly referred to as a dusty plasma. The levitated particles self-assemble into quasi two-dimensional (2D) crystalline clusters [49–51], yet these clusters remain intrinsically far from equilibrium. Fluctuations in the surrounding plasma, such as variations in electric field and particle charge, introduce stochastic forcing that excites particle oscillations [52–57]. In addition, their plasma-mediated interactions are intrinsically nonreciprocal. When ions stream past a negatively charged particle, they form an asymmetric region of enhanced ion density below the particle (ion wake), leading to effective forces that violate action-reaction symmetry [58–61]. There are several consequences of this nonreciprocity in dusty plasmas, including coupling between oscillation modes [62–65] and temperature gradients in nonreciprocally coupled layers [28].

In our experiments, we observe intermittent transitions between an ordered Coulomb cluster and an ergodic, gas-like state *without* external modulation. By tracking the full three-dimensional (3D) trajectories of all particles using laser-sheet tomography, we gain access to the complete phase space of the dynamics. Principal component analysis of the particle motion reveals that melting is triggered by a parametric excitation of a horizontal breathing mode, which is driven by vertical oscillations of the cluster. The nonreciprocal interactions between the particles break the discrete time-translation symmetry of the vertical oscillation mode, manifesting as a subharmonic frequency component relative to the vertical confinement frequency. Although stochastic noise alone can excite vertical motion, we show using simulations that nonrecip-

rocal interactions dramatically enhance the parametric mode-coupling by pumping the second harmonic of the breathing mode. This positive feedback loop drives an explosive growth in both horizontal and vertical modes that melts the cluster, which is not possible when the cluster is driven only by random noise.

Over long times, the simulations further show that introducing nonreciprocity induces intermittent dynamics characterized by abrupt melting events and bursts of kinetic energy, closely resembling the dynamics observed in experiments. In contrast, increasing noise merely raises the effective temperature uniformly without inducing intermittency marked by kinetic energy bursts. Together, these results demonstrate that our system offers a distinctive platform that links microscopic sources of nonreciprocity to the emergent dynamics of many-body systems. More broadly, we expect similar pathways of interaction-mediated activity to arise in other finite many-body systems and reshape their collective dynamics, from colloidal clusters to living cells to groups of animals.

II. EXPERIMENTAL SETUP

Figure 1(a) shows the experimental setup of the dusty plasma and the tomographic imaging system. A radio frequency (RF) power supply operating at 13.56 MHz is connected to an aluminum electrode (diameter = 15 cm). A thin copper ring (outer diameter = 8.2 cm, inner diameter = 6.4 cm, thickness = 0.2 cm) is placed at the center

of the electrode in order to generate the horizontal electrostatic confinement. A cylindrical neodymium magnet (diameter = 7.5 cm) is embedded inside the electrode and provides a nonuniform magnetic field ($B \approx 0.04$ T) that enhances the electrostatic confinement and drives a vertical flow of ions. The RF power was adjusted between 2-10 W, which was sufficient to sustain an argon plasma inside the vacuum chamber. The argon pressure varied between 0.8-1.2 Pa depending on experimental conditions, and was maintained throughout each experiment to within 1% using a feedback-controlled butterfly valve. Monodisperse melamine formaldehyde (MF) particles were released from a reservoir with a fine mesh at the top of the chamber. We used two batches of monodisperse particles with manufacturer-labeled diameters $10.55 \pm 0.14 \mu\text{m}$ and $12.8 \pm 0.32 \mu\text{m}$.

We tracked the motion of all particles in 3D using scanning laser sheet tomography [66]. As shown in Fig. 1(a), an oscillating laser sheet scans the system along the z -direction at 100-500 Hz. A high-speed camera operating at 4-20 kHz ensures that each scan cycle produces a stack of 40 images at distinct z positions (Fig. 1(b)). We then track the particles and reconstruct their trajectories in 3D using a custom implementation of TrackPy [67]. We apply a statistical method to reduce errors from pixel locking [68], especially in the z -direction where the resolution is limited by laser sheet width and scan frequency. Depending on the specific settings of camera resolution and laser scanning frequency, the ultimate resolution of each particle's position was 20-50 μm per pixel in the horizontal direction, and 50-100 μm per pixel in the z -direction.

III. FORCES IN DUSTY PLASMA

Particles experience several plasma-mediated forces, illustrated schematically in Fig. 1(c). In the plasma, particles are bombarded by free electrons and ions and become negatively charged due to the higher electron temperature (≈ 1.3 eV [55]). For the same reason, the electrode is also negatively charged, and forms a plasma sheath where the vertical electric field varies sharply in the z -direction. The electron and ion temperature and density also vary vertically in the sheath. Thus, the particle charge, $q(z)$, is position-dependent, which breaks translational symmetry in z . Particles are strongly confined at the edge of the plasma sheath, levitating approximately 1-2 cm above the electrode, where electrostatic repulsion balances gravity. In the horizontal direction, the electrode and copper ring provide a radial electric field that confines the particles.

In the sheath region, ions stream downward to the negatively-charged electrode. The horizontal component of the magnetic field deflects the streaming ions and induces a vertical flow in the azimuthal direction. As a result, the particles experience a vertical ion-drag force that drives cluster rotation [60]. The vertical component

of the ion drift velocity is orders of magnitude larger than the azimuthal component. Ions are also deflected when they stream past a negatively-charged particle, and form a wake structure of enhanced positive charge beneath each particle [61, 69-71]. The wake-mediated interaction is nonreciprocal: a particle sitting below another particle can be attracted to the wake of the upper one, whereas the upper particle is repelled [58, 59]. This nonreciprocity has been measured experimentally [58, 59], and its functional dependence on particle separations was recently extracted from experimental data using machine learning [60].

We summarize these interactions and (linearized) environmental forces in the following equations of motion. Let us denote the position of a particle $\mathbf{r}_i = (x_i, y_i, z_i)$ with $\boldsymbol{\rho}_i = (x_i, y_i)$, and the separation between two particles $\mathbf{r}_{ij} = \mathbf{r}_i - \mathbf{r}_j = \boldsymbol{\rho}_{ij} + (z_i - z_j)\hat{z}$, where $\boldsymbol{\rho}_{ij} = \rho_{ij}\hat{\boldsymbol{\rho}}_{ij} = (x_i - x_j, y_i - y_j)$. The equations of motion in the horizontal and vertical directions read:

$$\ddot{\boldsymbol{\rho}}_i = -\omega_h^2 \boldsymbol{\rho}_i + k_c^2 \hat{z} \times \boldsymbol{\rho}_i + \sum_{j \neq i} f_{ij}^h \hat{\boldsymbol{\rho}}_{ij} - \gamma_i \dot{\boldsymbol{\rho}}_i \quad (1)$$

$$\ddot{z}_i = -\omega_z^2 z_i + \sum_{j \neq i} f_{ij}^z - \gamma_i \dot{z}_i \quad (2)$$

where ω_h and ω_z are the horizontal and vertical confinement frequencies, and k_c describes the vortical ion flow. Dotted variables refer to time differentiation. f_{ij}^h and f_{ij}^z are the horizontal and vertical components of the reduced interaction force $\mathbf{f}_{ij}(\mathbf{r}_i, \mathbf{r}_j) = \mathbf{F}_{ij}(\mathbf{r}_i, \mathbf{r}_j)/m_i$, where m_i is the mass of particle i . Finally, γ_i is the damping coefficient, which depends on particle size. According to Epstein's law, for spherical MF particles with a density of $1510 \text{ kg}\cdot\text{m}^{-3}$ inside argon gas [72],

$$\gamma_i = \frac{12.2P}{d_i} \mu\text{m} \cdot \text{Pa}^{-1} \cdot \text{s}^{-1} \quad (3)$$

where d_i is the particle diameter and P is the argon pressure.

Because the particle charge varies with z , ω_h and F_{ij} are not invariant under translation in z , i.e., $\omega_h = \omega_h(z)$ and $\mathbf{F}_{ij} = \mathbf{F}_{ij}(\boldsymbol{\rho}_{ij}, z_i, z_j) \propto q_i(z_i)q_j(z_j)$. Furthermore, the forces are nonreciprocal, i.e. $\mathbf{F}_{ij} \neq -\mathbf{F}_{ji}$, meaning that pairwise forces not only differ in magnitude, but also do not point between the displacement vector, \mathbf{r}_{ij} . Therefore, vertical oscillations are intrinsically coupled to horizontal oscillations even when particles have zero vertical separation, and this is the origin of parametric coupling that eventually melts the clusters.

Once entering the plasma, two or more particles settle into a quasi-2D rotating crystalline structure, where the horizontal confinement force is balanced by repulsive interaction forces, and the azimuthal ion drag force is balanced by damping. Even though the rotating crystal is the equilibrium ground state, we observe that rotating crystals are not always stable, but instead undergo intermittent melting transitions. In the following, we analyze

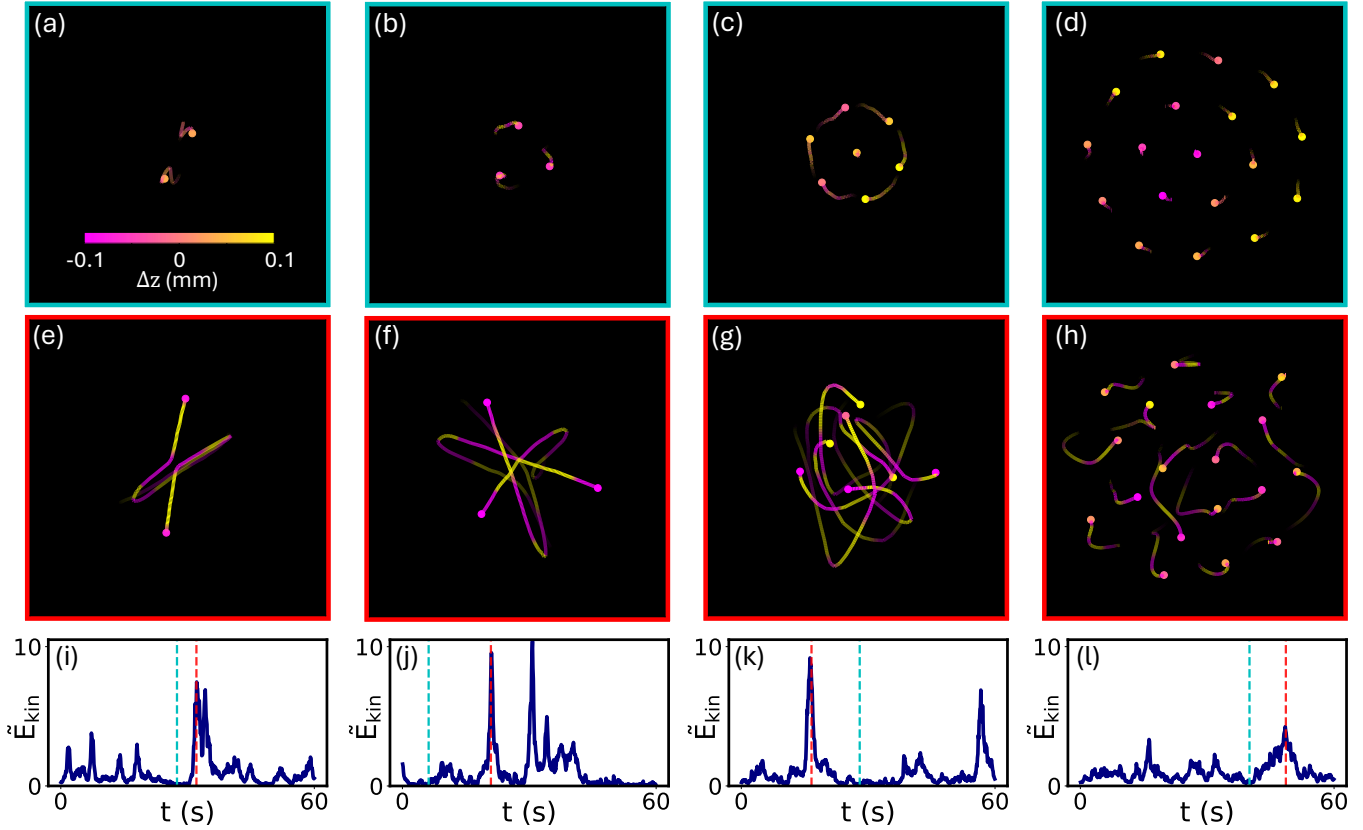


FIG. 2. Intermittent melting of Coulomb clusters composed of 2, 3, 7, and 18 particles. (a-d) 3D trajectories of the quiescent crystalline state of the clusters. The trajectories are plotted in the xy -plane over 0.25 s. The size of each panel is $4 \text{ mm} \times 4 \text{ mm}$. The z -coordinate of each particle is represented by the color of the traces, where $\Delta z = 0$ corresponds to the center of mass averaged over the whole time series. (e-h) 3D trajectories of the melted state of the clusters. (i-l) Total kinetic energy normalized by its time average over 60 s for each cluster. The blue (red) dashed line highlights the quiescent (melted) state shown above.

fluctuations away from these force-balanced configurations, and uncover how small oscillations are amplified to trigger melting transitions through a combined influence of stochastic noise and crucially, nonreciprocal interactions.

IV. RESULTS AND DISCUSSION

A. Intermittent melting of Coulomb clusters

Figure 2 shows four Coulomb clusters observed in our experiments undergoing intermittent melting over 60 seconds (Movie S1-S8 in Supplemental Material (SM) [73]). The 3D trajectories of the particles are plotted for both the quiescent state (Fig. 2(a-d)) and the melted state (Fig. 2(e-h)). The clusters stay in the quiescent state most of the time, where the motion is dominated by the uniform, rigid rotation of the cluster. The melting occurs intermittently, during which the kinetic energy increases dramatically. Surprisingly, the melting of clusters is not triggered by any externally applied modulations,

but rather occurs spontaneously. In all cases, melting is initiated by the excitation of a horizontal oscillation mode (Movies S1-S4 [73]). For clusters composed of 2, 3, and 7 particles, all particles (except the center one) oscillate radially with the same phase. For the 18-particle cluster, an asymmetric breathing mode is excited, where particles at the inner shell and outer shell oscillate radially, but with opposite phase.

The intermittent bursts of kinetic energy (Fig. 2(i-l)) are hallmarks of the nonequilibrium dynamics exhibited by these clusters. The timescale between bursts, typically of order tens of seconds, is much longer than any microscopic timescale, suggesting that the intermittency arises from collective dynamics. To understand the emergence of this intermittency, we first quantify the cluster's motion in its quiescent state, characterizing its rotation and oscillation modes, and then examine how these modes evolve as kinetic energy bursts develop.

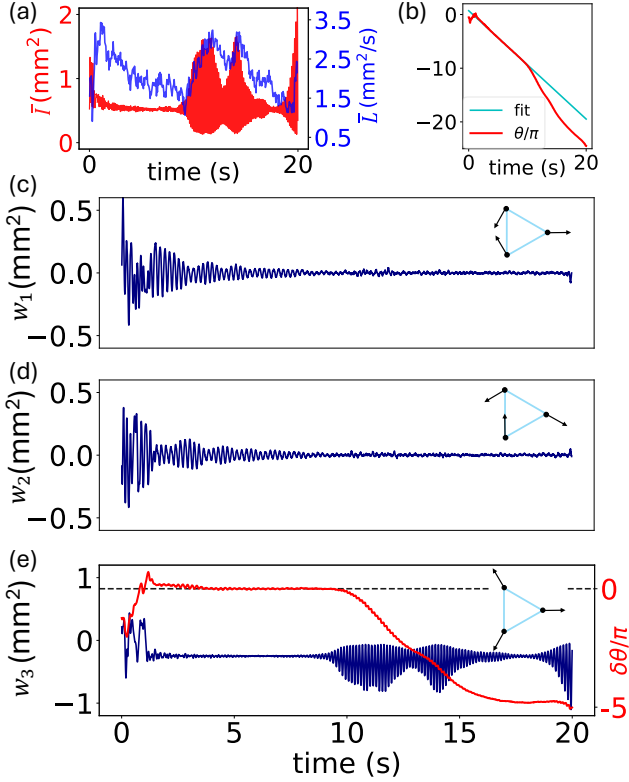


FIG. 3. Rotation and oscillation modes of the 3-particle cluster in experiments. (a) Reduced momentum of inertia \bar{I} , and reduced angular momentum \bar{L} . Both \bar{I} and \bar{L} increase when the breathing oscillation mode is excited. (b) Orientation angle of the cluster. The cyan line is a linear fit between $t = 4.5$ s to $t = 9.5$ s. (c-e) Evolution of the (w_1, w_2, w_3) variables. The insets show the corresponding displacements of the particles during the oscillation. The red data in (e) shows the deviation of θ from the linear fit in (b).

B. Three-particle cluster dynamics

We start our analysis on the simplest case with nontrivial oscillation modes: the three-particle cluster. In our experiments, the particles are nearly identical. However, they have slightly different masses that vary by a few percent and cannot be exactly determined. Thus we use the average manufacturer particle mass, m_0 , for each sample to compute cluster-wide properties. Figure 3(a) shows the reduced moment of inertia, $I/m_0 = \bar{I} = \sum_i \rho_i^2$, and the reduced angular momentum, $L/m_0 = \bar{L} = \sum_i \rho_i \times \dot{\rho}_i$, for the first 20 seconds of the experiment highlighted in Fig. 2(j). The oscillation of \bar{I} arises from the variation of cluster size associated with the breathing mode excitation. As evident in Eq. 1, \bar{L} is not conserved. If interactions are reciprocal, then the change of \bar{L} is determined by the torque due to the ion drag force and damping, leading to the following equation for \bar{L} :

$$\frac{d\bar{L}}{dt} = k_c^2 \bar{I} - \gamma \bar{L}. \quad (4)$$

Since we have assumed the particles are identical with mass m_0 , they have the same damping rate according to Eq. 3. \bar{L} increases with \bar{I} because particles experience a larger torque from ion drag force as they move farther away from the center of rotation [60, 74]. On the other hand, the negative torque from damping force increases with \bar{L} as the cluster rotates faster. Eq. (4) explains the initial relaxation of \bar{L} starting around $t = 2$ s, and its increase as \bar{I} increases. However, when the particles are not spaced symmetrically in the cluster, the nonreciprocal forces can lead to internal torques on the system, and Eq. (4) becomes invalid.

Ignoring the center of mass translation, the dynamics of a three-particle cluster in two dimensions are fully described by four variables: the orientation angle, θ , and three shape variables, w_1 , w_2 , and w_3 [75]. Here, θ is the angle between one edge of the triangular cluster and the x axis. The shape variables capture the amplitudes of three oscillation modes of the cluster: two degenerate bending modes, w_1 and w_2 , and the breathing mode, w_3 . When there is no oscillation and the cluster is an equilateral triangle, $w_1 = w_2 = 0$. The breathing mode variable is defined as

$$w_3 = \frac{1}{\sqrt{3}} (\rho_{13} \times \rho_{23}) \cdot \hat{z}, \quad (5)$$

where $\rho_{ij} = \rho_i - \rho_j$. The magnitude of w_3 is proportional to the area of the triangle formed by the cluster, while its sign encodes the permutation parity of the three particles (w_3 switches sign whenever the ordering of the particles reverse). Therefore, switching between positive and negative values serves as a good indicator of cluster melting.

Figures 3(b–e) show the evolution of the orientation angle and the shape variables for the first 20 seconds of the experiment. Recording starts at $t = 0$ s, immediately after a melting event, when the cluster was relaxing back to the quiescent state. During the quiescent state, (w_1, w_2, w_3) return to their equilibrium values, and θ varies linearly in time. A deviation of $\theta(t)$ from a linear fit emerges at $t \approx 10$ s, marking the onset of the breathing mode excitation with a concomitant increase in the oscillation of w_3 . During the excitation, the deviation between $\theta(t)$ and its linear fit continues to grow, revealing that the cluster rotates faster when the breathing mode is excited. The accelerated rotation can be understood simply by considering conservation of angular momentum during a single oscillation with $\bar{L} \neq 0$, where small radial oscillations of a non-rigid body can cause global rotation. In contrast, if $\bar{L} = 0$, excitation of the breathing mode cannot induce rotation; instead, global rotation is driven by the excitation of w_1 and w_2 when they are out of phase [75].

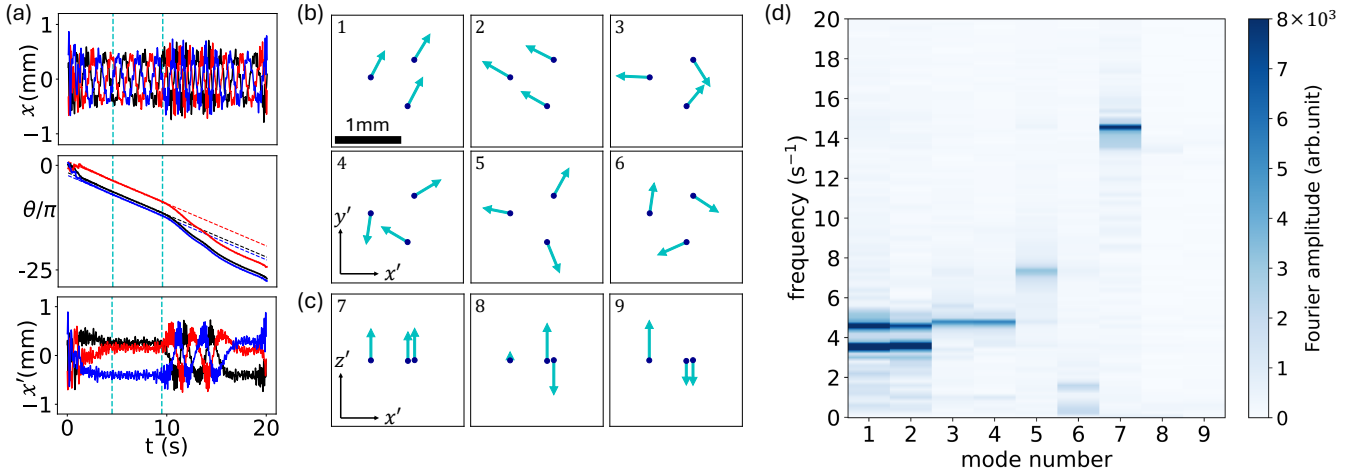


FIG. 4. PCA mode analysis of the 3-particle cluster experiment in the rotating reference frame. (a) The x -coordinate of each particle (red, blue, black) in the laboratory frame oscillates due to rotation. The rotation angle of each particle varies linearly until the breathing mode is excited. The 5 s region between the vertical cyan dashed lines denote the quiescent state where the angular velocity of the rotating frame is computed. In the rotating frame (x'), the positions are fixed prior to the breathing mode excitation. (b, c) Oscillation modes from PCA in the horizontal (1-6) and vertical (7-9) directions. Modes 1 and 2 are center of mass translations. Modes 3 and 4 are the two degenerate vibrating modes (w_1 and w_2). Mode 5 is the breathing oscillation, and mode 6 is the zero-frequency rotational mode. Mode 7 is the z center of mass oscillation, and modes 8-9 are asymmetric vertical oscillations. The length of the arrows denote relative displacements of the particles. (d) Fourier spectrum of the PCA modes. Modes 1 and 2 have split peaks due to the Coriolis force. The vertical fluctuations are dominated by mode 7, whose frequency is approximately twice the breathing mode 5.

C. PCA extraction of oscillation modes

While the dynamics of a three-particle cluster can be described compactly using the shape variables, a more general approach is required to extract oscillation modes in larger clusters. We therefore apply principal component analysis (PCA) as an unbiased method for identifying collective modes directly from experimental data [76, 77], and to reveal parametric coupling between modes that lead to melting. The workflow is summarized in Fig. 4.

PCA extracts orthogonal modes from the covariance of particle position fluctuations around an equilibrium configuration. The first step is to obtain the equilibrium configuration by removing the global rotation (Fig. 4(a)). We first estimate the angular velocity, Ω , of the rigid rotation during the quiescent state by measuring the angular velocities of individual particles about the center of mass, and taking the average. Particle coordinates are then transformed into the rotating frame via $\rho'(t) = \mathbf{R} \cdot \rho(t)$ where $\mathbf{R}(\theta)$ is the rotation matrix about the z axis, and $\theta = \Omega t$. In the rotating frame, Eq. 1 becomes:

$$\ddot{\rho}'_i = -(\omega_h^2 - \Omega^2)\rho'_i - 2\Omega\hat{\mathbf{z}} \times \dot{\rho}'_i + \sum_{j \neq i} f_{ij}^h \hat{\rho}'_{ij} - \gamma_i \dot{\rho}'_i - (\gamma_i \Omega - k_c^2) \hat{\mathbf{z}} \times \rho'_i. \quad (6)$$

This transformation has a few consequences. The effective confinement potential is reduced due to the centrifugal force, and the Coriolis force is non-negligible. The

vortical force disappears when damping is balanced with the ion drag force. In this frame, particles fluctuate around fixed equilibrium positions without rotation when the cluster is in the quiescent state (Movie S9 [73]).

We construct separate covariance matrices for the fluctuations of the horizontal and vertical coordinates in the rotating frame (see SM [73]). The eigenvectors of these matrices decompose the positional fluctuations into different oscillation modes, and the eigenvalues correspond to the contribution of each mode to the fluctuations about equilibrium. For the three-particle cluster, PCA identifies 6 horizontal modes, illustrated in Fig. 4(b). There are two center of mass translational modes, two bending modes, the breathing mode, and the rotational mode. In addition, there are three vertical modes shown in Fig. 4(c). Particle trajectories are projected onto each mode to obtain the corresponding time series of mode amplitudes, and the mode spectra are obtained by performing Fourier transforms on each time series, as shown in Fig. 4(d). The two translation modes are degenerate and have two peaks that correspond to $\omega_h \pm \Omega$. This frequency splitting results directly from the Coriolis force in the rotating reference frame (see SM [73]). The two bending modes are also degenerate as expected, while the breathing mode is the highest frequency horizontal mode. The bending modes and the breathing mode agree well with those described by the (w_1, w_2, w_3) variables. Additionally, in the vertical direction, the particle motion is dominated by the center of mass translation mode.

This analysis demonstrates that PCA can serve as a re-

liable method of extracting oscillation modes from particle trajectories measured in experiments. While here we emphasize the 3-particle system for simplicity, PCA works equally well on larger clusters, for example, 7 particles (Figs. S1 and S2), and 18 particles (Figs. S3 and S4), as shown in SM [73].

D. Parametric coupling drives melting

Among all modes, two play a central role in the melting dynamics: the horizontal breathing mode and the vertical center of mass mode. In Fig. 5(a), we plot the average cluster radius $R = \frac{1}{3} \sum_i \sqrt{x_i^2 + y_i^2}$, which quantitatively indicates the breathing mode amplitude, and the vertical center of mass position z_{com} . Transitions between shaded and unshaded regions indicate where w_3 switches sign, and melting corresponds to densely-spaced transitions. In the melted state, both R and z_{com} exhibit large-amplitude fluctuations, and increase simultaneously before melting occurs (Fig. 5(b)). In Fig. 5(c), spectral analysis shows that the breathing mode has a peak frequency $f_b = 7.42 \text{ s}^{-1}$, while the vertical center of mass mode has a peak frequency $f_z = 14.57 \text{ s}^{-1}$, nearly twice the breathing mode frequency. This 2:1 frequency ratio is indicative of a parametric coupling: the breathing mode is parametrically modulated by the vertical oscillation. Such parametric coupling is consistently observed in all experiments where melting occurs, and is absent in experiments where the cluster remains quiescent (Figs. S5 and S6 [73]).

Parametric instability exists ubiquitously in periodically modulated systems. Common examples include Faraday waves: vertically shaking a flat fluid interface at frequency ω_D can excite standing surface waves with frequency $\omega_D/2$ [78]. The instability can be modeled by an oscillator coordinate q whose fundamental frequency, ω_0 , is periodically modulated at frequency ω_D , resulting in a damped Mathieu equation:

$$\ddot{q} + \omega_0^2[1 + \epsilon \cos(\omega_D t)]q + \lambda\dot{q} = 0, \quad (7)$$

where λ is the damping rate. When ω_D is close to $2\omega_0/n$ (n is a positive integer), the solution will grow exponentially when the coupling strength ϵ exceeds a threshold [79]. In our Coulomb clusters, the parametric coupling between horizontal and vertical oscillation modes originates from the particles' charge dependence on vertical position in the plasma sheath [52–55]. The equilibrium charge of a particle depends on the local electron and ion density, and local plasma potential, all of which vary sharply in z . The oscillation modes of a cluster are determined by the dynamical matrix, which includes interactions between the particles, and the interactions depend on the charge of each particle. Therefore, the frequencies of the horizontal oscillation modes of the cluster are modulated by the charge variation as the cluster oscillates vertically. It is thus possible to selectively excite

certain oscillation modes given that the vertical oscillation of the cluster is driven at about twice the desired horizontal mode frequency, for example, through a sinusoidal AC driving signal applied at the electrode [80].

In contrast, the clusters in our experiment are not subject to any external periodic driving. The particles spontaneously oscillate in the vertical direction with small amplitude, typically less than 0.5 mm, which is two orders of magnitude larger than expected from thermal Brownian motion. The oscillations are likely due to a finite charging time as particles move through the plasma sheath, or a fluctuating background plasma environment [52, 53, 55]. If the vertical oscillation amplitude is larger than the threshold for parametric growth, the horizontal mode can be excited. However, this mode amplification is difficult to sustain since nonlinearity typically alters the mode frequency and stops the mode from growing further. Yet, we observe explosive melting preceded by simultaneous growth of the breathing and vertical center of mass modes (Fig. 5(b)). As we will show, nonreciprocal interactions between the particles are necessary to sustain the parametric instability.

E. Parametric pumping enhanced by nonreciprocal interactions

By breaking reciprocity, the sum of the interaction forces in the system can be nonzero and act as an effective driving force on the system's center of mass. This is evident in the Fourier spectrum of the center of mass oscillation of the cluster (Fig. 5(c)), where besides the peak vertical confinement frequency at $f_z = 14.57 \text{ s}^{-1}$, there is a subharmonic peak near $f_z/2$. This subharmonic peak breaks the discrete time-translational symmetry of the vertical oscillation due to confinement, as if the cluster is driven by an additional external force. As we will show below, this effective driving force originates from the nonreciprocal interactions between particles, and is crucial in enhancing the parametric instability and producing large amplitude oscillations that lead to melting.

1. Simulating nonreciprocal Coulomb clusters

To elucidate the role of nonreciprocity, we performed simulations of our Coulomb clusters using a custom molecular dynamics code [60]. The details of the simulation are described in Appendix A, and here we give a brief summary. Each simulation consists of three nearly identical spherical particles with diameters $10.51 \mu\text{m}$, $10.55 \mu\text{m}$, and $10.59 \mu\text{m}$, consistent with size variations in the experiment. In the horizontal plane, the particles are confined in a harmonic trap mimicking the electric field in the experiment. The particles also experience a vortical ion drag force which induces the rotation. In the vertical direction, the particles are subject to a linearly varying electric field, and gravity. The electrostatic force

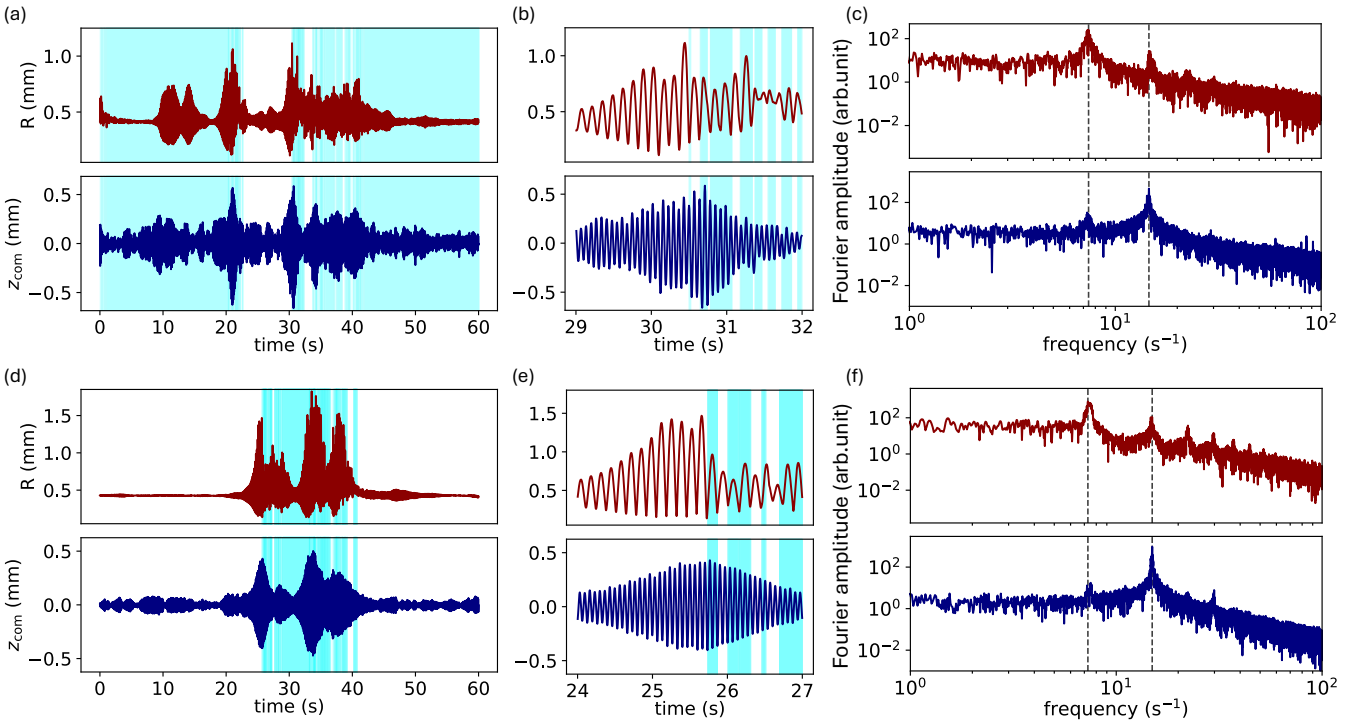


FIG. 5. Simultaneous growth of the horizontal breathing mode and vertical center of mass mode drives melting in both experiment (a-c) and simulation with $\tilde{q} = 0.4$, $\sigma = 0.1$. (d-f) Cluster radius, R , and the z center of mass, z_{com} , of the 3-particle cluster. The blue shaded regions indicate $w_3 < 0$. (b,e) R and z_{com} of the 3-particle cluster near the onset of melting. The breathing mode amplitude increases until the cluster melts and w_3 begins to switch sign. The amplitude of the z center of mass oscillation grows with the breathing mode. (c,f) Fourier spectrum of R and z_{com} . The two dashed lines mark the peak frequencies of $f_b = 7.42 \text{ s}^{-1}$ (7.28 s^{-1}), and $f_z = 14.57 \text{ s}^{-1}$ (14.95 s^{-1}) in experiment (simulation).

is determined by the field strength multiplied by the particle charge.

In the simulation, the negative charge of a particle increases in magnitude as the particle moves downward. The particles themselves interact through a Yukawa potential with a screening length $\lambda_D = 0.45 \text{ mm}$. This interaction is reciprocal, however, it does not include interactions with the ion wakes beneath each particle (Fig. 1), which are nonreciprocal. We model the ion wake as a cloud of positive charge attached a distance of $0.3\lambda_D$ below each particle and moves with the particle as if the cloud is massless [28, 60, 81]. The amount of charge carried by the positive charge cloud is $\tilde{q}|q_0|$, where q_0 is the charge of the particle at position $z = 0$, and \tilde{q} is a dimensionless constant. To recover reciprocal interactions, \tilde{q} can be set to zero. Finally, Gaussian noise of standard deviation σ is added in the vertical acceleration for each particle at each simulation step to roughly model the stochastic fluctuations that drive spontaneous vertical oscillations of the particles.

The simulations show excellent quantitative agreement with the experiments, as illustrated in Fig. 5(d-f) (Movie S10 [73]). The breathing mode is spontaneously excited, and its amplitude grows dramatically leading to cluster melting. When the breathing mode is excited, the ver-

tical oscillation amplitude increases correspondingly, far exceeding the amplitude due to Gaussian noise. In the Fourier spectrum of z_{com} , a subharmonic peak exists near $f_z/2$, suggesting the breaking of discrete time translational symmetry of the vertical confinement. In comparison, we also perform simulations with purely reciprocal interactions (see Appendix A). In this case, the breathing mode excitation and cluster melting can still occur, but require unphysical amounts of stochastic noise, resulting in vertical oscillation amplitudes exceeding those observed in experiments. Importantly, the subharmonic peak in the spectrum of z_{com} is absent.

2. Nonreciprocity-enhanced parametric pumping

To elucidate how nonreciprocal interactions from ion wakes enhance the parametric instability, we examine the simulation immediately before a melting event. Figure 6(a) shows the growth of R during the excitation of the breathing mode. We calculate the total interaction force (divided by the average mass) acting on the cluster in the vertical direction during this process: $f_{\text{int}}^z = \sum_{i \neq j} \mathbf{f}_{ij} \cdot \hat{\mathbf{z}}$. For reciprocal interactions, $f_{\text{int}}^z = 0$ because $\mathbf{f}_{ij} + \mathbf{f}_{ji} = 0$ for any pair of identical particles. In

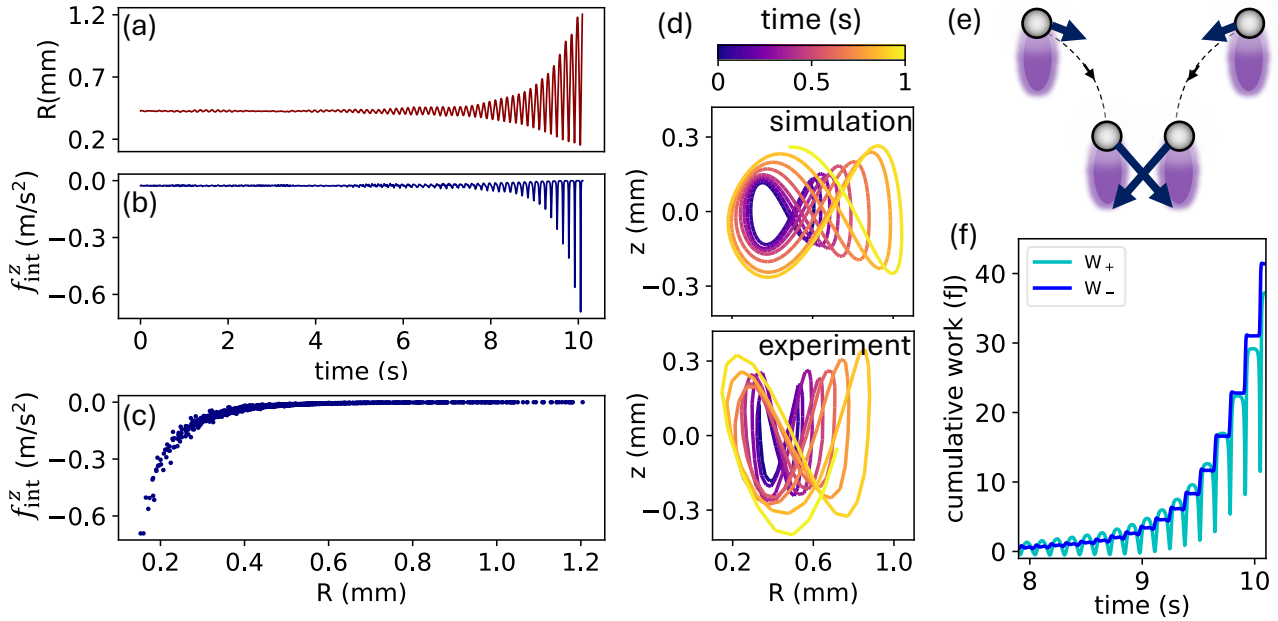


FIG. 6. Nonreciprocal interactions drive vertical oscillations and enhance parametric pumping. (a-b) Cluster size (R) and z -component of the total interaction force (f_{int}^z) during excitation of the breathing mode in simulation with $\tilde{q} = 0.4$, $\sigma = 0.1$. (c) f_{int}^z as a function of R during the same time period. (d) Trajectories of R and z_{com} during a breathing mode excitation in both simulation and experiment. (e) Illustration showing that attraction to ion wakes in the z -direction drives the vertical oscillation during each cycle of the breathing mode. (f) Cumulative work W_{\pm} done by the two components of the interaction forces, as defined in the text.

contrast, as shown in Fig. 6(b), f_{int}^z is not zero, remains predominantly negative, and oscillates in phase with the breathing mode. Moreover, its magnitude increases substantially as the breathing mode amplitude grows. In Fig. 6(c) we plot f_{int}^z versus R . At small R , the vertical interaction force is strongly enhanced, whereas it approaches zero at large R . Thus, the total z -force on the system depends directly on the breathing mode amplitude.

We visualize the parametric pumping by plotting the trajectory of the cluster in the (R, z_{com}) phase space. Figure 6(d) shows representative trajectories over a one-second interval prior to melting for both simulation and experiment. Owing to the parametric coupling between the two modes, the trajectories form a characteristic figure-eight shape whose size increases as the instability develops. Nonreciprocal interactions enhance this coupling, as sketched in Fig. 6(e): when particles approach each other during the breathing motion, they experience a stronger attraction toward the ion wakes of neighboring particles, resulting in a larger net downward force on the cluster center of mass. Consequently, the breathing mode effectively drives vertical oscillations at f_b through the nonreciprocal interaction force f_{int}^z . This is the origin of the subharmonic peak in the Fourier spectrum of z_{com} (Fig. 5(c) and 5(f)).

Energetically, nonreciprocal interactions enhance the parametric instability by enabling a unidirectional chan-

nelling of energy into the system. To show this, we decompose the interaction force into two components: $\mathbf{F}_+^{ij} = \frac{1}{2}(\mathbf{F}_{ij} - \mathbf{F}_{ji})$ and $\mathbf{F}_-^{ij} = \frac{1}{2}(\mathbf{F}_{ij} + \mathbf{F}_{ji})$. For reciprocal interactions, $\mathbf{F}_+^{ij} = \mathbf{F}_{ij}$ and $\mathbf{F}_-^{ij} = 0$. In Fig. 6(f), we plot the cumulative work done by each component, $W_{\pm}(t) = \int_0^t \sum_{i \neq j} \mathbf{F}_{\pm}^{ij} \cdot \mathbf{v}_i dt'$. Since \mathbf{F}_+^{ij} is dominated by Coulomb repulsion, W_+ alternates between doing positive and negative work on the cluster during each breathing mode cycle, with small bias towards positive work due to the growth of the oscillation amplitude. In contrast, W_- unidirectionally pumps energy into the cluster through the mechanism depicted in Fig. 6(e). We note that for reciprocal interactions, $W_- = 0$. Besides sourcing energy from the environment during each breathing mode cycle, we will also show that f_{int}^z directly drives vertical oscillations near resonance at $2f_b$, dramatically enhancing the growth of the breathing mode amplitude and melting the cluster.

3. A minimal model for nonreciprocal parametric pumping

The mechanism by which nonreciprocal interactions enhance the growth of the breathing mode and induce cluster melting can be captured by a minimal model consisting of two parametrically coupled modes with nonreciprocal feedback. First, mode 1 is parametrically modulated by mode 2, such that the excitation of mode 1

depends on the amplitude of mode 2, as in conventional parametric coupling. Second, nonreciprocal interactions produce a driving force that depends on mode 1 and drives mode 2, thereby closing a positive feedback loop between the two modes. Consider two oscillators, x_1 and x_2 with natural frequencies ω_1 and ω_2 , respectively, and damping rate γ . The frequency ω_1 is modulated by the oscillation of x_2 through the coupling parameter δ . x_2 is driven by a sinusoidal force on resonance and a feedback force f which depends on x_1 . The equations of motion read:

$$\begin{aligned}\ddot{x}_1 + \omega_1^2(1 + \delta x_2)x_1 + \gamma\dot{x}_1 &= 0, \\ \ddot{x}_2 + \omega_2^2x_2 + \gamma\dot{x}_2 &= a \cos(\omega_2 t) + f(x_1).\end{aligned}\quad (8)$$

The displacements x_1 and x_2 represent the horizontal breathing mode and the vertical center of mass mode, respectively. While in reality, the vertical oscillation is driven by stochastic noise or other plasma-specific fluctuations, here we drive x_2 with a sinusoidal force for simplicity.

In the absence of $f(x_1)$, x_2 oscillates with a fixed amplitude in steady state, $x_2(t) = a/\gamma\omega_2 \sin(\omega_2 t)$. When $\omega_2 \approx 2\omega_1$, for large enough driving amplitude a , x_1 can grow exponentially. Assume x_1 oscillates at frequency ω_1 with a slowly varying amplitude: $x_1 = \frac{1}{2}A(t)e^{i\omega_1 t} + \frac{1}{2}A^*(t)e^{-i\omega_1 t}$. Then $A \propto e^{g_0 t}$, and the growth rate is given by :

$$g_0 = -\frac{\gamma}{2} + \sqrt{\left(\frac{a\delta\omega_1}{4\gamma\omega_2}\right)^2 - \frac{\Delta^2}{4}}, \quad (9)$$

where $\Delta = \omega_2 - 2\omega_1$. The feedback force $f(x_1)$ captures the nonzero total interaction force in the vertical direction, which depends on the breathing mode as shown in Fig. 6(c). Note that $f(0) = 0$ because we subtract the value of f_{int}^z at equilibrium R so that $x_2 = 0$ represents the equilibrium position of the vertical center of mass of the cluster. Expanding $f(x_1)$ near the horizontal equilibrium position $x_1 = 0$ yields (Fig. S7 [73]):

$$f(x_1) = f_1 x_1 + f_2 x_1^2 + \mathcal{O}(x_1^3). \quad (10)$$

The linear term $f_1 x_1$ generate a component of the feedback force oscillating near ω_1 , producing the subharmonic peak at ω_1 in the vertical oscillation (Fig. 5(f)). The quadratic term $f_2 x_1^2$ play a crucial role: it generates a component of the feedback force oscillating near $2\omega_1$, which drives x_2 near resonance. As a result, the amplitude of x_2 is no longer fixed by the external drive alone, but instead increases with the breathing mode amplitude, leading to a self-enhancing parametric instability.

Writing $x_1 = \frac{1}{2}A(t)e^{i\omega_1 t} + \frac{1}{2}A^*(t)e^{-i\omega_1 t}$ and $x_2 = \frac{1}{2}B(t)e^{i\omega_2 t} + \frac{1}{2}B^*(t)e^{-i\omega_2 t}$, and applying the rotating wave approximation, we obtain the amplitude equations (see Appendix B):

$$\dot{A} = -\frac{\gamma}{2}A - i\frac{\Delta}{2}A + \frac{i\delta\omega_1}{4}BA^* \quad (11a)$$

$$\dot{B} = -\frac{\gamma}{2}B + \frac{a}{2i\omega_2} + \frac{f_2}{4i\omega_2}A^2. \quad (11b)$$

Although the resulting amplitude equation is nonlinear and determining the full time evolution is challenging, it remains possible to define an instantaneous growth rate that captures the local amplification of the breathing mode amplitude:

$$\begin{aligned}g_{\text{inst}} &= \frac{d}{dt} \ln |A| = \frac{1}{2} \frac{d}{dt} \ln |A|^2 = \frac{1}{2|A|^2} \frac{d|A|^2}{dt} \\ &= \frac{1}{|A|^2} \text{Re}[\dot{A}A^*] = -\frac{\gamma}{2} + \frac{\delta\omega_1}{4} \text{Re} \left[iB \frac{(A^*)^2}{|A|^2} \right].\end{aligned}\quad (12)$$

To solve for B , we assume the following initial conditions: $|A(0)| \ll 1$, $\dot{A}(0) = 0$ and $B(0) = a/(i\gamma\omega_2)$, i.e. at $t = 0$, x_2 is in the steady state in response to the sinusoidal driving $a \cos(\omega_2 t)$. Integrating Eq.(11b) gives

$$B(t) = B(0) + \frac{f_2}{4i\omega_2} e^{-\frac{\gamma}{2}t} \int_0^t e^{\frac{\gamma}{2}t'} A^2(t') dt'. \quad (13)$$

In the usual parametric instability, $A(t)$ grows exponentially. Here, due to the feedback force $f(x_1)$, $A(t)$ is expected to grow with an increasing growth rate. Nevertheless, in order to evaluate Eq.(13), we assume $A(t)$ grows with a fixed bare growth rate g_0 , i.e. $A(t) \approx A(0)\exp(g_0 t)$. Eq.(13) then gives

$$\begin{aligned}B(t) &\approx B(0) + \frac{f_2 A^2(0)}{4i\omega_2} e^{-\frac{\gamma}{2}t} \int_0^t e^{(2g_0 + \frac{\gamma}{2})t'} dt' \\ &= \frac{a}{i\gamma\omega_2} + \frac{f_2 A^2(0)}{4i\omega_2(2g_0 + \gamma/2)} \left(e^{2g_0 t} - e^{-\frac{\gamma}{2}t} \right) \\ &\approx \frac{a}{i\gamma\omega_2} + \frac{f_2 A^2(t)}{4i\omega_2(2g_0 + \gamma/2)}.\end{aligned}\quad (14)$$

Plugging this into Eq.(12) gives (see Appendix B)

$$g_{\text{inst}} = g_0 + \frac{\delta\omega_1 f_2 |A|^2}{16\omega_2(2g_0 + \gamma/2)} \quad (15)$$

Equation (15) highlights the central effect of nonreciprocal feedback—unlike the baseline parametric instability, where the growth rate is controlled by a fixed external drive (Fig. S8 [73]), the parametric modulation here increases with the breathing-mode amplitude through the feedback force, $f_2 x_1^2$. The instability is thus self-enhancing, leading to a substantially larger growth rate. In Fig. 7(a), we numerically solve Eq. (8) and plot the instantaneous growth rate of x_1 as a function of its amplitude $|A|$ (the parameters used for the minimal model are listed in the SM [73]). The numerical results match the analytical prediction (Eq. (15)) exceedingly well and verify the quadratic dependence on $|A|$. In experiments, the explosive growth is cut off by the eventual melting of the Coulomb cluster (Fig. S9 and Fig. S10 [73]). In the melted state, well-defined vibrational modes no longer exist, and drag forces from the neutral gas eventually allow for reformation of the cluster.

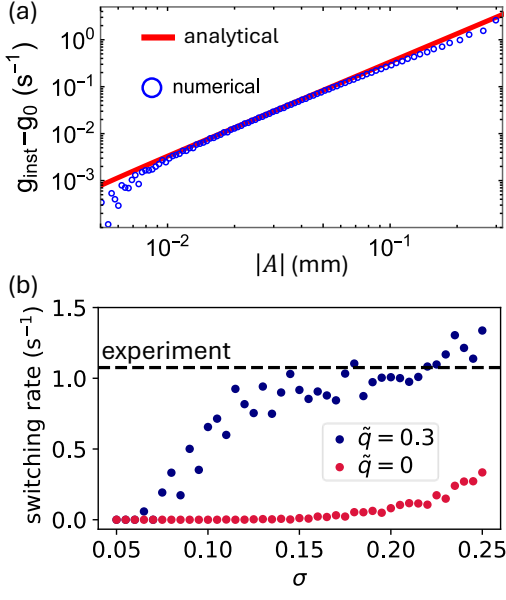


FIG. 7. Nonreciprocity induces explosive mode growth and abrupt transitions to melting. (a) Instantaneous growth rate of x_1 (subtracting the bare growth rate g_0) from the minimal model. Numerical results come from solving Eq. 8 directly, and the analytical prediction is given in Eq. 15. (b) Switching rate of w_3 versus noise strength σ for simulations with reciprocal ($\tilde{q} = 0$) and nonreciprocal ($\tilde{q} = 0.3$) interactions. The black dashed line represent the switching rate observed in the three-particle experiment (Fig. 2j)

F. Nonreciprocity rewrites intermittency statistics

We have shown that nonreciprocal interactions dramatically enhance the parametric pumping of the breathing mode and induce cluster melting. In the melted state, w_3 rapidly switches between negative and positive values (Eq. 5). Therefore, its switching rate quantifies how often melting occurs. Figure 7(b) shows the average switching rate of w_3 , defined as the number of sign changes of w_3 divided by the total simulation (experiment) time, for simulations with reciprocal and nonreciprocal interactions at different noise strengths (σ). For reciprocal interactions, the switching rate increases gradually with σ . However, even for large noise ($\sigma = 0.25$), the switching rate remains significantly lower than the experimental value. In contrast, with nonreciprocal interactions, the switching rate increases much more rapidly with noise and approaches the experimental value at around $\sigma = 0.15$.

The parametric pumping relies on spatial symmetry of the cluster, where all particles move in unison (breathing mode). During the melted state, this mechanism no longer exists, kinetic energy is removed through damping, and the cluster re-forms. Over long times, the melting/recrystallization cycles are intermittent, and display distinct dynamics due to nonreciprocal interactions. To demonstrate this, we performed extensive simulations over a range of noise strength (σ)

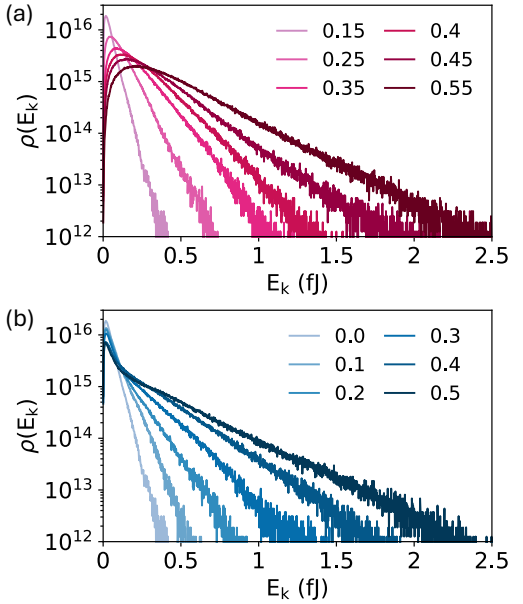


FIG. 8. Stochastic noise and nonreciprocity increase kinetic energy in different ways. (a) Probability distribution of kinetic energy for simulations with reciprocal interactions. Increasing the noise level (σ is indicated in the legend) uniformly increases the temperature. (b) Probability distribution of kinetic energy for simulations at noise level $\sigma = 0.15$. Increasing the nonreciprocity (\tilde{q} is indicated in the legend) results in two distinct regimes corresponding to quiescent and melted states.

and nonreciprocity (\tilde{q}). Figure 8 shows the probability distributions of the total cluster kinetic energy, E_k , obtained from these simulations. In the absence of nonreciprocity (Fig. 8(a)), increasing σ simply thermalizes the system, leading to a higher effective temperature and a kinetic energy distribution consistent with a Maxwell-Boltzmann (MB) velocity distribution, $\rho(E_k) \propto \sqrt{E_k}(k_B T)^{-3/2} \exp(-E_k/k_B T)$, where k_B is the Boltzmann constant and T is the effective temperature. In contrast, for a fixed noise strength (Fig. 8(b)), increasing \tilde{q} produces two distinct regimes: a peak at low energies (quiescent periods), and a high-energy tail corresponding to melted states. This indicates strong deviations from equilibrium statistics.

These distinct kinetic energy distributions reflect qualitatively different intermittent dynamics induced by nonreciprocal interactions. Figures 9(a) and 9(b) show representative time series of R and E_k over 200 s for simulations with reciprocal and nonreciprocal interactions, respectively. The two simulations produce states with intermittent variations in R and similar average kinetic energy, but E_k is intermittent only when nonreciprocal interactions are present. With nonreciprocity, the vertical center of mass mode increases concomitantly with the breathing mode (Fig. 5(d)), whereas the vertical mode is roughly insensitive to the breathing mode with reciprocal interactions (Fig. A1 in Appendix A). Since the vertical

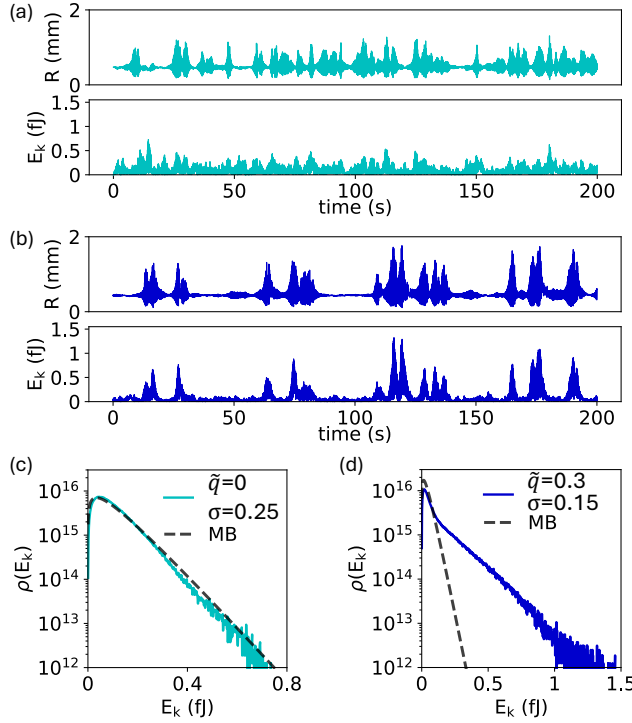


FIG. 9. Nonreciprocal interactions induce punctuated bursts of kinetic energy. (a,b) Time series of average cluster radius and total kinetic energy from simulations with $\tilde{q} = 0, \sigma = 0.25$ (a) and $\tilde{q} = 0.3, \sigma = 0.15$ (b). (c) Kinetic energy probability distribution with noise only. The data is well-fit by a MB energy distribution with $T \approx 5 \times 10^6$ K and $\langle E_k \rangle = 0.102$ fJ. (d) Kinetic energy probability distribution with nonreciprocity. The dashed line is an MB fit for a simulation with the same noise strength but $\tilde{q} = 0$, giving $T \approx 2 \times 10^6$ K. The average kinetic energy is $\langle E_k \rangle = 0.118$ fJ.

mode carries a significant fraction of the kinetic energy, the system-wide dynamics are intermittent. Figure 9(c-d) shows probability distributions of the kinetic energy in each case. In the absence of nonreciprocity, the breathing mode is excited by large random noise. The fluctuation of kinetic energy is determined by the noise strength, and its distribution is well-fit by a MB energy distribution. However, even at substantially lower noise strength, nonreciprocal interactions facilitate a unidirectional injection of energy into the system during parametric coupling. This results in intermittent bursts of global kinetic energy that closely resemble those observed experimentally, and consequently a strongly nonequilibrium energy distribution with two regimes and high-energy tails.

V. CONCLUSIONS

We have experimentally demonstrated that nonreciprocal interactions strongly enhance the parametric instability between two oscillation modes in a Coulomb clus-

ter, ultimately driving the cluster melting. Unlike conventional parametric pumping induced by external driving, where the instability is controlled by the driving strength, here nonreciprocal interactions act as an emergent internal driving mechanism that enables unidirectional energy injection into the cluster. As a result, the system enters an intermittent nonequilibrium state characterized by alternations between quiescent crystalline phases and melted, ergodic phases. Through simulations incorporating nonreciprocal interactions, we reproduce intermittent melting dynamics that closely resemble those observed in experiments, and confirm that such intermittency is absent when the system is driven solely by random noise.

Beyond Coulomb clusters, our results identify a pathway by which strongly-coupled many-body systems can sustain dynamical nonequilibrium behavior through activity originated from microscopic nonreciprocity. Unlike conventional active matter, where energy is injected at the level of individual constituents, the activity here is mediated by nonreciprocal interactions and emerges collectively at the level of coupled modes. Similar forms of interaction-mediated activity arise naturally in a variety of physical systems, including colloidal assemblies in acoustic and light fields [30, 32–34], and mechanical metamaterials [19], where state manipulation through parametric pumping could benefit from such emergent activity [82, 83]. Moreover, living systems often involve both single particle activity from energy consumption, and field-mediated interactions, i.e., hydrodynamics or chemical cues, that can facilitate collective motions such as flocking and schooling [23]. How the interplay between activity and nonreciprocal (and possibly nonpairwise) interactions shapes collective behavior requires further exploration. Therefore, our results highlight how nonreciprocity-induced emergent activity—here realized through parametric coupling between two oscillation modes—can play an important role in a broad class of strongly-coupled, many-body systems.

ACKNOWLEDGMENTS

This material is based upon work supported by the NSF under award numbers 2010524 and 2409416, and by the Gordon and Betty Moore Foundation, Grant DOI 10.37807/gbmf12256.

Appendix A: Dusty plasma simulations

We simulate particle dynamics in dusty plasmas using a custom molecular dynamics code [60]. The simulations consist of spherical particles with radii d_i and masses $m_i = \rho_p \pi d_i^3 / 6$, where $\rho_p = 1510 \text{ kg} \cdot \text{m}^{-3}$. In the horizontal direction, particles experience environmental forces due to a harmonic confinement potential, ion drag

force, and damping. The reduced forces acting on particle i located at (x_i, y_i) read:

$$f_{i,x}^{\text{env}} = (1+b)\chi_h q_i x_i/m_i + k_c^2 y_i - \gamma_i \dot{x}_i \quad (\text{A1})$$

$$f_{i,y}^{\text{env}} = (1-b)\chi_h q_i y_i/m_i - k_c^2 x_i - \gamma_i \dot{y}_i \quad (\text{A2})$$

The dimensionless parameter b describes the degree of asymmetry of the horizontal confinement, χ_h is the horizontal electric field gradient, q_i is the charge of particle i , k_c describes the vortical ion drag force, and γ_i is the damping rate due to Epstein drag.

In the vertical direction, the particles experience forces due to a linearly-varying electric field, gravity, damping, and stochastic noise:

$$f_{i,z}^{\text{env}} = \min(E_0 + \chi_v z_i, 0) q_i/m_i - g - \gamma_i \dot{z}_i + \eta(t) g. \quad (\text{A3})$$

χ_v is the vertical electric field gradient, E_0 is the electric field at $z_i = 0$, and the **min** function ensures that the vertical electric field is never positive. The vertical electric field becomes zero at $z = -E_0/\chi_v$, where the plasma sheath ends. $g = 9.81 \text{ m} \cdot \text{s}^{-2}$ is the gravitational acceleration. Finally, $\eta(t)$ is a Wiener process with zero mean and variance σ^2 . We refer to the standard deviation σ as the noise strength. The charge of each particle also changes with vertical position, which is crucial for parametric coupling. We model the particles as spherical capacitors, with charge varying linearly in z and a maximum set by the floating potential in bulk plasma:

$$q_i = \min(2\pi\epsilon_0 d_i V(1 - z_i/l_q), -8 \times 10^{-16} \text{ C}), \quad (\text{A4})$$

where $V = -8.14 \text{ V}$ and $l_q = 1.5 \text{ mm}$. Linearizing these environmental forces gives the environmental forces in Eq. 1 and Eq. 2 (excluding the asymmetry b). Thus, we can relate the parameters of the electric fields in simulation to confinement frequencies to match experiments.

Due to the ion wakes, the interactions between particles are nonreciprocal. We model the ion wake as a cloud of positive charge with magnitude $\tilde{q}|q|$ attached at a distance h below the particle. The interaction force exerted by particle j on particle i can be expressed as $\mathbf{F}_{ij} = -\nabla_i \varphi(\mathbf{r}_{ij})$ where

$$\varphi(\mathbf{r}) = \frac{q_i q_j}{4\pi\epsilon_0 \lambda_D} \left[\frac{e^{-r/\lambda_D}}{r/\lambda_D} - \frac{\tilde{q} e^{-r_w/\lambda_D}}{\frac{r_w}{\lambda_D} \left(1 + c \frac{e^{-r_w/\lambda_D}}{r_w/\lambda_D} \right)} \right]. \quad (\text{A5})$$

$r_w = |\mathbf{r} - h\hat{z}|$ is the distance between particle i and the wake of particle j , λ_D is the Debye length and c is a dimensionless parameter to ensure the potential does not diverge in the limit r_w goes to 0. The equations of motion for the particles under the influence of environmental and interaction forces are integrated over time using second order velocity Verlet method.

In the main text we have discussed the dynamics in simulations with nonreciprocity. Here we add the results

for purely reciprocal interactions. Figure A1 shows time series of R and z_{com} and their Fourier spectrum, for a simulation with $\tilde{q} = 0$ and $\sigma = 0.25$. Although melting occurs, the excitation of the breathing mode no longer drives the vertical oscillation. As shown in Fig. A1(b), the vertical oscillation amplitude stays approximately constant while the breathing mode amplitude grows significantly. In the Fourier spectrum of z_{com} , there is no subharmonic peak near the breathing mode frequency, which is in contradiction with the experiment.

Appendix B: Amplitude-dependent growth rate in the minimal model

In the following, we provide the details of the derivation of the instantaneous growth rate Eq.(15). We start from the equations of motion:

$$\begin{aligned} \ddot{x}_1 + \omega_1^2(1 + \delta x_2)x_1 + \gamma \dot{x}_1 &= 0, \\ \ddot{x}_2 + \omega_2^2 x_2 + \gamma \dot{x}_2 &= a \cos(\omega_2 t) + f(x_1), \end{aligned} \quad (\text{B1})$$

where

$$f(x_1) = f_1 x_1 + f_2 x_1^2 + \mathcal{O}(x_1^3). \quad (\text{B2})$$

We write $x_1 = \frac{1}{2}A(t)e^{i\omega_1 t} + \frac{1}{2}A^*(t)e^{-i\omega_1 t}$ and $x_2 = \frac{1}{2}B(t)e^{i\omega_2 t} + \frac{1}{2}B^*(t)e^{-i\omega_2 t}$. Using rotating wave approximation to keep terms near resonance with x_1 and x_2 , together with the following approximations $\dot{x}_1 \approx -\frac{1}{2}\omega_1^2 A e^{i\omega_1 t} + i\omega_1 \dot{A} e^{i\omega_1 t} + \text{c.c.}$, $\dot{x}_2 \approx -\frac{1}{2}\omega_2^2 B e^{i\omega_2 t} + i\omega_2 \dot{B} e^{i\omega_2 t} + \text{c.c.}$, $\gamma/\omega_1 \ll 1$ (c.c. represents complex conjugate), we get

$$\dot{A} = -\frac{\gamma}{2}A + \frac{i\delta\omega_1}{4}BA^*e^{i\Delta t} \quad (\text{B3a})$$

$$\dot{B} = -\frac{\gamma}{2}B + \frac{a}{2i\omega_2} + \frac{f_2}{4i\omega_2}A^2e^{-i\Delta t} \quad (\text{B3b})$$

where $\Delta = \omega_2 - 2\omega_1$. We can eliminate the $e^{i\Delta t}$ dependence by making the transformation $A \rightarrow Ae^{i\Delta t/2}$ and get

$$\dot{A} = -\frac{\gamma}{2}A - \frac{i\Delta}{2}A + \frac{i\delta\omega_1}{4}BA^* \quad (\text{B4a})$$

$$\dot{B} = -\frac{\gamma}{2}B + \frac{a}{2i\omega_2} + \frac{f_2}{4i\omega_2}A^2. \quad (\text{B4b})$$

Assuming $A(t)$ grows with the constant bare growth rate g_0 , we obtained the expression for $B(t)$ in Eq.(14):

$$B(t) \approx \frac{a}{i\gamma\omega_2} + \frac{f_2 A^2(t)}{4i\omega_2(2g_0 + \gamma/2)}. \quad (\text{B5})$$

Plugging this into Eq.(12) gives the instantaneous growth rate of the amplitude of x_1 :

$$\begin{aligned} g_{\text{inst}} &= \frac{d}{dt} \ln |A| = -\frac{\gamma}{2} + \frac{\delta\omega_1}{4} \text{Re} \left[iB \frac{(A^*)^2}{|A|^2} \right] \\ &= -\frac{\gamma}{2} + \frac{a\delta\omega_1}{4\gamma\omega_2} \cos 2\phi + \frac{\delta\omega_1 f_2 |A|^2}{16\omega_2(2g_0 + \gamma/2)}, \end{aligned} \quad (\text{B6})$$

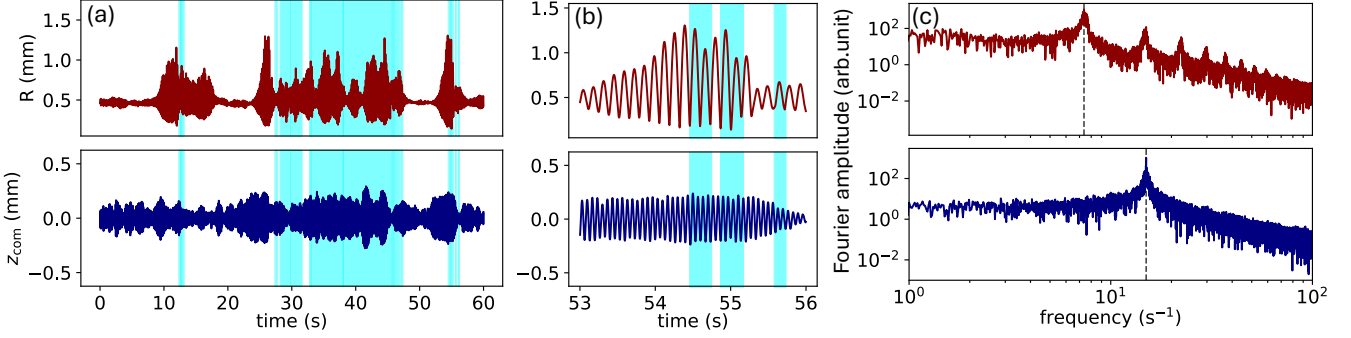


FIG. A1. Simulation of 3 particles with the same masses as Fig. 5(b) and reciprocal interactions ($\tilde{q} = 0, \sigma = 0.25$). (a) Time series of R and z_{com} . (b) R and z_{com} near the melting. The breathing mode grows significantly and induces melting, but the vertical oscillation amplitude stays nearly constant. (c) Fourier spectrum of R and z_{com} . The subharmonic peak is absent from the spectrum of z_{com} .

where ϕ is the phase of the amplitude of x_1 : $A = |A|e^{i\phi}$. To determine $\cos 2\phi$, we plug Eq.(B5) into Eq.(B4a):

$$|\dot{A}|e^{i\phi} + i\dot{\phi}|A|e^{i\phi} = -\frac{\gamma}{2}|A|e^{i\phi} - i\frac{\Delta}{2}|A|e^{i\phi} + \frac{a\delta\omega_1}{4\gamma\omega_2}|A|e^{-i\phi} + \frac{\delta\omega_1 f_2}{16\omega_2(2g_0 + \gamma/2)}|A|^3 e^{i\phi}. \quad (\text{B7})$$

By multiplying $e^{-i\phi}$ on both sides and taking the imaginary part of this equation, we get

$$\dot{\phi} = -\frac{\Delta}{2} - \frac{a\delta\omega_1}{4\gamma\omega_2} \sin 2\phi. \quad (\text{B8})$$

ϕ has a stationary solution $\dot{\phi} = 0$ when $|\frac{a\delta\omega_1}{4\gamma\omega_2}| > |\frac{\Delta}{2}|$, from which we can determine $\cos 2\phi$:

$$\cos 2\phi = \sqrt{1 - (\sin 2\phi)^2} = \sqrt{1 - \left(\frac{2\gamma\omega_2\Delta}{a\delta\omega_1}\right)^2} \quad (\text{B9})$$

Here, the decision to assume $\cos 2\theta > 0$ is justified because we require a positive growth rate when $|A| \ll 1$. Plugging Eq.(B9) into Eq.(B6) gives Eq.(15):

$$g_{\text{inst}} = -\frac{\gamma}{2} + \sqrt{\left(\frac{a\delta\omega_1}{4\gamma\omega_2}\right)^2 - \frac{\Delta^2}{4}} + \frac{\delta\omega_1 f_2 |A|^2}{16\omega_2(2g_0 + \gamma/2)} \quad (\text{B10})$$

[1] M. J. Bowick, N. Fakhri, M. C. Marchetti, and S. Ramaswamy, Symmetry, thermodynamics, and topology in active matter, *Physical Review X* **12**, 010501 (2022).

[2] C. Battle, C. P. Broedersz, N. Fakhri, V. F. Geyer, J. Howard, C. F. Schmidt, and F. C. MacKintosh, Broken detailed balance at mesoscopic scales in active biological systems, *Science* **352**, 604 (2016).

[3] M. Schliwa and G. Woehlke, Molecular motors, *Nature* **422**, 759 (2003).

[4] F. Jülicher, A. Ajdari, and J. Prost, Modeling molecular motors, *Reviews of Modern Physics* **69**, 1269 (1997).

[5] M. Ballerini, N. Cabibbo, R. Candelier, A. Cavagna, E. Cisbani, I. Giardina, V. Lecomte, A. Orlandi, G. Parisi, A. Procaccini, *et al.*, Interaction ruling animal collective behavior depends on topological rather than metric distance: Evidence from a field study, *Proceedings of the national academy of sciences* **105**, 1232 (2008).

[6] A. Cavagna, A. Cimarelli, I. Giardina, G. Parisi, R. Santagati, F. Stefanini, and M. Viale, Scale-free correlations in starling flocks, *Proceedings of the National Academy of Sciences* **107**, 11865 (2010).

[7] M. Nagy, Z. Ákos, D. Biro, and T. Vicsek, Hierarchical group dynamics in pigeon flocks, *Nature* **464**, 890 (2010).

[8] F. Ginelli, F. Peruani, M.-H. Pillot, H. Chaté, G. Theraulaz, and R. Bon, Intermittent collective dynamics emerge from conflicting imperatives in sheep herds, *Proceedings of the National Academy of Sciences* **112**, 12729 (2015).

[9] J. Palacci, S. Sacanna, A. P. Steinberg, D. J. Pine, and P. M. Chaikin, Living crystals of light-activated colloidal surfers, *Science* **339**, 936 (2013).

[10] A. Aubret, M. Youssef, S. Sacanna, and J. Palacci, Targeted assembly and synchronization of self-spinning microgears, *Nature Physics* **14**, 1114 (2018).

[11] A. Bricard, J.-B. Caussin, N. Desreumaux, O. Dauchot, and D. Bartolo, Emergence of macroscopic directed motion in populations of motile colloids, *Nature* **503**, 95 (2013).

[12] A. Bricard, J.-B. Caussin, D. Das, C. Savoie, V. Chikkadi, K. Shitara, O. Chepizhko, F. Peruani, D. Saintillan, and D. Bartolo, Emergent vortices in populations of colloidal rollers, *Nature communications* **6**, 7470 (2015).

[13] T. Lefranc, A. Dinelli, C. Fernández-Rico, R. P. Dullens, J. Tailleur, and D. Bartolo, Synthetic quorum sensing

and absorbing phase transitions in colloidal active matter, *Physical Review X* **15**, 031050 (2025).

[14] S. Maity and A. Morin, Spontaneous demixing of binary colloidal flocks, *Physical Review Letters* **131**, 178304 (2023).

[15] S. Osat and R. Golestanian, Non-reciprocal multifarious self-organization, *Nature Nanotechnology* **18**, 79 (2023).

[16] S. Osat, J. Metson, M. Kardar, and R. Golestanian, Escaping kinetic traps using nonreciprocal interactions, *Physical Review Letters* **133**, 028301 (2024).

[17] C. Scheibner, A. Souslov, D. Banerjee, P. Surówka, W. T. Irvine, and V. Vitelli, Odd elasticity, *Nature Physics* **16**, 475 (2020).

[18] P. Baconnier, D. Shohat, C. H. López, C. Coulais, V. Démery, G. Düring, and O. Dauchot, Selective and collective actuation in active solids, *Nature Physics* **18**, 1234 (2022).

[19] J. Veenstra, C. Scheibner, M. Brandenbourger, J. Binysh, A. Souslov, V. Vitelli, and C. Coulais, Adaptive locomotion of active solids, *Nature* **639**, 935 (2025).

[20] M. Brandenbourger, X. Locsin, E. Lerner, and C. Coulais, Non-reciprocal robotic metamaterials, *Nature communications* **10**, 4608 (2019).

[21] J. Veenstra, O. Gamayun, X. Guo, A. Sarvi, C. V. Meinersen, and C. Coulais, Non-reciprocal topological solitons in active metamaterials, *Nature* **627**, 528 (2024).

[22] J. Veenstra, O. Gamayun, M. Brandenbourger, F. van Gorp, H. Terwisscha-Dekker, J.-S. Caux, and C. Coulais, Nonreciprocal breathing solitons, *Physical Review X* **15**, 031045 (2025).

[23] M. C. Marchetti, J.-F. Joanny, S. Ramaswamy, T. B. Liverpool, J. Prost, M. Rao, and R. A. Simha, Hydrodynamics of soft active matter, *Reviews of modern physics* **85**, 1143 (2013).

[24] C. Bechinger, R. Di Leonardo, H. Löwen, C. Reichhardt, G. Volpe, and G. Volpe, Active particles in complex and crowded environments, *Reviews of modern physics* **88**, 045006 (2016).

[25] H. C. Berg and D. A. Brown, Chemotaxis in *Escherichia coli* analysed by three-dimensional tracking, *Nature* **239**, 500 (1972).

[26] W. F. Paxton, K. C. Kistler, C. C. Olmeda, A. Sen, S. K. St. Angelo, Y. Cao, T. E. Mallouk, P. E. Lammert, and V. H. Crespi, Catalytic nanomotors: autonomous movement of striped nanorods, *Journal of the American Chemical Society* **126**, 13424 (2004).

[27] R. Golestanian, T. B. Liverpool, and A. Ajdari, Propulsion of a molecular machine by asymmetric distribution of reaction products, *Physical review letters* **94**, 220801 (2005).

[28] A. V. Ivlev, J. Bartnick, M. Heinen, C.-R. Du, V. Nosenko, and H. Löwen, Statistical mechanics where Newton's third law is broken, *Physical Review X* **5**, 011035 (2015).

[29] S. A. Loos and S. H. Klapp, Irreversibility, heat and information flows induced by non-reciprocal interactions, *New Journal of Physics* **22**, 123051 (2020).

[30] E. M. King, M. C. Morrell, J. B. Sustiel, M. Gronert, H. Pastor, and D. G. Grier, Scattered waves fuel emergent activity, *Physical Review Research* **7**, 013055 (2025).

[31] M. C. Morrell, L. Elliott, and D. G. Grier, Nonreciprocal wave-mediated interactions power a classical time crystal, *arXiv preprint arXiv:2504.15495* (2025).

[32] B. Wu, Q. Mao, B. VanSaders, and H. M. Jaeger, Nonreciprocity and multibody interactions in acoustically levitated particle systems: A three-body problem, *Physical Review E* **112**, 035410 (2025).

[33] N. St. Clair, D. Davenport, A. D. Kim, and D. Kleckner, Dynamics of acoustically bound particles, *Physical Review Research* **5**, 013051 (2023).

[34] J. Parker, S. Nagasamudram, C. Peterson, Y. Li, S. Soleimanikahnoj, S. A. Rice, and N. F. Scherer, Symmetry breaking-induced n-body electrodynamic forces in optical matter systems, *Nature Communications* **16**, 6294 (2025).

[35] A. U. Oza, L. Ristroph, and M. J. Shelley, Lattices of hydrodynamically interacting flapping swimmers, *Physical Review X* **9**, 041024 (2019).

[36] A. Filella, F. Nadal, C. Sire, E. Kanso, and C. Eloy, Model of collective fish behavior with hydrodynamic interactions, *Physical Review Letters* **120**, 198101 (2018).

[37] T. H. Tan, A. Mietke, J. Li, Y. Chen, H. Higinbotham, P. J. Foster, S. Gokhale, J. Dunkel, and N. Fakhri, Odd dynamics of living chiral crystals, *Nature* **607**, 287 (2022).

[38] S. Saha, J. Agudo-Canalejo, and R. Golestanian, Scalar active mixtures: The nonreciprocal cahn-hilliard model, *Physical Review X* **10**, 041009 (2020).

[39] Z. You, A. Baskaran, and M. C. Marchetti, Nonreciprocity as a generic route to traveling states, *Proceedings of the National Academy of Sciences* **117**, 19767 (2020).

[40] M. Fruchart, R. Hanai, P. B. Littlewood, and V. Vitelli, Non-reciprocal phase transitions, *Nature* **592**, 363 (2021).

[41] F. Brauns and M. C. Marchetti, Nonreciprocal pattern formation of conserved fields, *Physical Review X* **14**, 021014 (2024).

[42] Y. Avni, M. Fruchart, D. Martin, D. Seara, and V. Vitelli, Nonreciprocal ising model, *Physical Review Letters* **134**, 117103 (2025).

[43] T. Nadolny, C. Bruder, and M. Brunelli, Nonreciprocal synchronization of active quantum spins, *Physical Review X* **15**, 011010 (2025).

[44] D. Martin, D. Seara, Y. Avni, M. Fruchart, and V. Vitelli, Transition to collective motion in nonreciprocal active matter: Coarse graining agent-based models into fluctuating hydrodynamics, *Physical Review X* **15**, 041015 (2025).

[45] D. J. Hickey, R. Golestanian, and A. Vilfan, Nonreciprocal interactions give rise to fast cilium synchronization in finite systems, *Proceedings of the National Academy of Sciences* **120**, e2307279120 (2023).

[46] S. Guillet, A. Poncet, M. Le Blay, W. T. Irvine, V. Vitelli, and D. Bartolo, Melting of nonreciprocal solids: How dislocations propel and fission in flowing crystals, *Proceedings of the National Academy of Sciences* **122**, e2412993122 (2025).

[47] Z. Zhang and R. Garcia-Millan, Entropy production of nonreciprocal interactions, *Physical Review Research* **5**, L022033 (2023).

[48] B.-q. Ai, Brownian motors powered by nonreciprocal interactions, *Physical Review E* **108**, 064409 (2023).

[49] H. Thomas, G. Morfill, V. Demmel, J. Goree, B. Feuerbacher, and D. Möhlmann, Plasma crystal: Coulomb crystallization in a dusty plasma, *Physical Review Letters* **73**, 652 (1994).

[50] J. Chu and I. Lin, Direct observation of coulomb crystals and liquids in strongly coupled rf dusty plasmas, *Physical*

review letters **72**, 4009 (1994).

[51] W.-T. Juan, Z.-H. Huang, J.-W. Hsu, Y.-J. Lai, *et al.*, Observation of dust coulomb clusters in a plasma trap, *Physical Review E* **58**, R6947 (1998).

[52] S. Nunomura, T. Misawa, N. Ohno, and S. Takamura, Instability of dust particles in a coulomb crystal due to delayed charging, *Physical review letters* **83**, 1970 (1999).

[53] A. Ivlev, U. Konopka, and G. Morfill, Influence of charge variation on particle oscillations in the plasma sheath, *Physical Review E* **62**, 2739 (2000).

[54] A. Douglass, V. Land, K. Qiao, L. Matthews, and T. Hyde, Determination of the levitation limits of dust particles within the sheath in complex plasma experiments, *Physics of Plasmas* **19** (2012).

[55] J. Méndez Harper, G. Gogia, B. Wu, Z. Laseter, and J. C. Burton, Origin of large-amplitude oscillations of dust particles in a plasma sheath, *Physical Review Research* **2**, 033500 (2020).

[56] G. Gogia and J. C. Burton, Emergent bistability and switching in a nonequilibrium crystal, *Physical Review Letters* **119**, 178004 (2017).

[57] G. Gogia, W. Yu, and J. C. Burton, Intermittent turbulence in a many-body system, *Physical Review Research* **2**, 023250 (2020).

[58] A. Melzer, V. Schweigert, and A. Piel, Transition from attractive to repulsive forces between dust molecules in a plasma sheath, *Physical review letters* **83**, 3194 (1999).

[59] G. A. Hebner, M. Riley, and B. Marder, Dynamic probe of dust wakefield interactions using constrained collisions, *Physical Review E* **68**, 016403 (2003).

[60] W. Yu, E. Abdelaleem, I. Nemenman, and J. C. Burton, Physics-tailored machine learning reveals unexpected physics in dusty plasmas, *Proceedings of the National Academy of Sciences* **122**, e2505725122 (2025).

[61] L. S. Matthews, D. L. Sanford, E. G. Kostadinova, K. S. Ashrafi, E. Guay, and T. W. Hyde, Dust charging in dynamic ion wakes, *Physics of Plasmas* **27** (2020).

[62] L. Couëdel, V. Nosenko, A. Ivlev, S. Zhdanov, H. Thomas, and G. Morfill, Direct observation of mode-coupling instability in two-dimensional plasma crystals, *Physical review letters* **104**, 195001 (2010).

[63] B. Liu, J. Goree, and Y. Feng, Mode coupling for phonons in a single-layer dusty plasma crystal, *Physical review letters* **105**, 085004 (2010).

[64] Z. Ding, K. Qiao, N. Ernst, J. Kong, M. Chen, L. S. Matthews, and T. W. Hyde, Nonlinear mode coupling and internal resonance observed in a dusty plasma, *New Journal of Physics* **21**, 103051 (2019).

[65] S. Zhdanov, A. Ivlev, and G. Morfill, Mode-coupling instability of two-dimensional plasma crystals, *Physics of Plasmas* **16** (2009).

[66] W. Yu and J. C. Burton, 3d tracking of particles in a dusty plasma by laser sheet tomography, *Physics of Plasmas* **30** (2023).

[67] D. B. Allan, T. Caswell, N. C. Keim, C. M. van der Wel, and R. W. Verweij, [soft-matter/trackpy](#): Trackpy v0.5.0 (v0.5.0) (2021).

[68] S. Burov, P. Figlizzzi, B. Lin, S. A. Rice, N. F. Scherer, and A. R. Dinner, Single-pixel interior filling function approach for detecting and correcting errors in particle tracking, *Proceedings of the National Academy of Sciences* **114**, 221 (2017).

[69] S. V. Vladimirov and M. Nambu, Attraction of charged particulates in plasmas with finite flows, *Physical Review E* **52**, R2172 (1995).

[70] O. Ishihara and S. V. Vladimirov, Wake potential of a dust grain in a plasma with ion flow, *Physics of Plasmas* **4**, 69 (1997).

[71] M. Lampe, G. Joyce, G. Ganguli, and V. Gavrishchaka, Interactions between dust grains in a dusty plasma, *Physics of Plasmas* **7**, 3851 (2000).

[72] P. S. Epstein, On the resistance experienced by spheres in their motion through gases, *Physical Review* **23**, 710 (1924).

[73] See Supplemental Information.

[74] W. Yu, J. Cho, and J. C. Burton, Extracting forces from noisy dynamics in dusty plasmas, *Physical Review E* **106**, 035303 (2022).

[75] O. Saporta Katz and E. Efrati, Self-driven fractional rotational diffusion of the harmonic three-mass system, *Physical review letters* **122**, 024102 (2019).

[76] S. Chen, C. W. Peterson, J. A. Parker, S. A. Rice, A. L. Ferguson, and N. F. Scherer, Data-driven reaction coordinate discovery in overdamped and non-conservative systems: application to optical matter structural isomerization, *Nature Communications* **12**, 2548 (2021).

[77] Y. Ivanov and A. Melzer, Melting dynamics of finite clusters in dusty plasmas, *Physics of plasmas* **12** (2005).

[78] J. Miles and D. Henderson, Parametrically forced surface waves, *Annual Review of Fluid Mechanics* **22**, 143 (1990).

[79] I. Kovacic, R. Rand, and S. Mohamed Sah, Mathieu's equation and its generalizations: overview of stability charts and their features, *Applied Mechanics Reviews* **70**, 020802 (2018).

[80] V. Yaroshenko and G. Morfill, Parametric excitation of low frequency waves in complex (dusty) plasmas, *Physics of Plasmas* **9**, 4495 (2002).

[81] N. P. Kryuchkov, L. A. Mistryukova, A. V. Sapelkin, and S. O. Yurchenko, Strange attractors induced by melting in systems with nonreciprocal effective interactions, *Physical Review E* **101**, 063205 (2020).

[82] Q. Mao, B. Wu, B. VanSaders, and H. M. Jaeger, Structural reconfiguration of interacting multi-particle systems through parametric pumping, *Nature communications* **16**, 4637 (2025).

[83] S. Shi, M. C. Hübl, G. Grosjean, C. P. Goodrich, and S. Waitukaitis, Electrostatics overcome acoustic collapse to assemble, adapt, and activate levitated matter, *Proceedings of the National Academy of Sciences* **122**, e2516865122 (2025).